JOURNAL OF AIRCRAFT
Vol. 39, No. 5, September–October 2002

Limit-Cycle Hysteresis Response for a High-Aspect-Ratio Wing Model

Deman Tang* and Earl H. Dowell†
Duke University, Durham, North Carolina 27708-0300

An experimental high-aspect-ratio wing aeroelastic model with a slender body at the tip has been constructed, and the response due to flutter and limit-cycle oscillations (LCOs) has been measured in a wind-tunnel test. A theoretical model has been developed and calculations made to correlate with the experimental data. Structural equations of motion based on nonlinear beam theory are combined with the ONERA aerodynamic stall model to study the LCO hysteresis phenomenon of a high-aspect-ratio wing model. Time simulation and a harmonic balance approach are each used to compute the LCO hysteretic response. The results between the theory and experiment are in good agreement.

Introduction

AEROELASTIC stability and limit-cycle oscillation response of an aircraft with a high-aspect-ratio wing have been studied for many years for subsonic to supersonic flow. Most investigators have used linear beam theory to simplify the wing structural model. As shown in Refs. 1–3, however, a geometric structural nonlinearity may arise from the coupling between elastic flap bending, chordwise bending, and torsion for very high-aspect-ratio wings typical of uninhabited air vehicles (UAV). In Refs. 2 and 3, the effect of the large static preflutter deformation on the flutter boundary and limit-cycle oscillation response has been studied. The results provide additional insight with respect to the contribution of structural nonlinear coupling to the aeroelastic stability and response of high-aspect-ratio wings.

Following Refs. 1–4, an experimental and theoretical study on flutter, limit-cycle oscillations (LCOs) and gust response of high-aspect-ratio wings has been reported in Refs. 5 and 6. An experimental high-aspect-ratio wing aeroelastic model with a tip slender body was constructed, and a wind-tunnel test conducted to measure the static aeroelastic response, flutter, and LCO[5] for a horizontally mounted wing. Large static preflutter deformations in the vertical or the torsional direction were created by the gravity loading on the wing and a tip slender body and also by a steady angle of attack, which provided a static aerodynamic load on the wing. In Ref. 6, the wing model was mounted vertically to eliminate gravity effects. Large static preflutter deformations were only created by a steady angle of attack. The discussion was focused on the nonlinear gust response. The experimental results of Refs. 5 and 6 largely validate the theoretical results of earlier studies.[2–4] Note an LCO hysteresis phenomenon was found from both the time simulation and the experimental observation of the nonlinear aeroelastic system in Refs. 5 and 6.

Following the work of Refs. 5 and 6, in the present paper we develop a mathematical model and computational code using the harmonic balance method to calculate the LCO response of a high-aspect-ratio wing at low subsonic flow speeds. A special focus is on the hysteretic response. The harmonic balance results complement earlier results from time simulations and provide additional insight with respect to the contribution of structural nonlinear coupling to the aeroelastic stability and response of high-aspect-ratio wings.

Strip theory aerodynamics has been used in the present work; although this is well validated for high-aspect-ratio wings with attached flow, less is known about the accuracy of strip theory when flow separation occurs.

Harmonic Balance Method

An experimental high-aspect-ratio wing model with a slender body at the tip has been described in Ref. 5. Large static preflutter deformations in the vertical or torsional direction are created by the gravity loading on the wing and a tip slender body. Figure 1 shows a photograph of the experimental model in the wind tunnel.

The wing is of constant chord, $c = 5.08$ cm, and span, $l = 45.08$ cm. The airfoil section is a NACA 0012. The bending and torsional stiffness of the wing is provided by a beam internal to the aerodynamic shape. It is rectangular in cross section of 1.27 cm width and 0.127 cm thickness and made of steel (precision ground).

The state-space equations based on the Hodges–Dowell[1] equations, ONERA stall aerodynamic model,[7] and the Galerkin method have been derived in Ref. 5. The results are given by

$$[\mathcal{A}]\{\dot{q}\} + [\mathcal{B}]\{q\} = \{F_0\} + \{F_N\} \tag{1}$$

where $\{q\}$ is a state vector, which is defined as

$$\{q\} = \{\dot{V}_j, V_j, \dot{W}_j, W_j, \dot{\Phi}, \Phi_j, C_{ll}, C_{ml}, C_{dl}\}$$

V_j, W_j, and Φ_j are the generalized coordinates in chordwise, flapwise, and torsional directions. C_{ll}, C_{ml}, and C_{dl} are the ONERA airfoil aerodynamic coefficients. The structural mode number is $j = 1, 2, \ldots, N$, and the aerodynamic section number along the span of the wing is $l = 1, 2, \ldots, NN$. The coefficient matrices $[\mathcal{A}]$ and $[\mathcal{B}]$ are dependent on the flow and structural parameters. The force vectors $\boldsymbol{F}_0$ and $\boldsymbol{F}_N$ are static force obtained from the effects of gravity and the nonlinear forces obtained from the structural nonlinearity and stall aerodynamics, respectively.

A harmonic balance approach can be derived using Eq. (1). Here, we consider a modal vector $\{X\}$ composed of the structural generalized coordinates $\{W_j, V_j, \Phi_j\}$. All quantities are cast into their first harmonic forms, that is,

$$X(U, \theta_0, g) = X_0 + X_s \sin\omega t + X_c \cos\omega t \tag{2}$$

where

$$\{X_0\} = \{V_{j0}, W_{j0}, \Phi_{j0}\}, \qquad \{X_s\} = \{V_{js}, W_{js}, \Phi_{js}\}$$

$$\{X_c\} = \{V_{jc}, W_{jc}, \Phi_{jc}\}$$

Received 18 May 2001; revision received 22 May 2002; accepted for publication 29 May 2002.

*Research Associate Professor, Department of Mechanical Engineering and Materials Science.

†J. A. Jones Professor, Department of Mechanical Engineering and Materials Science, Director of the Center for Nonlinear and Complex Systems, and Dean Emeritus, Pratt School of Engineering.

Table 1 Aerodynamic coefficients

Coefficients	Lift	Moment
a_{0z}	$5.9\ \text{rad}^{-1}$	0
s_z	$0.09\times 180/\pi\ \text{rad}^{-1}$	$-\pi/4\ \text{rad}^{-1}$
k_{vz}	$\pi/2\ \text{rad}^{-1}$	$-3\pi/16\ \text{rad}^{-1}$
λ_z	0.15	0
α_z	0.55	1
σ_z	$5.9\ \text{rad}^{-1}$	$-\pi/4\ \text{rad}^{-1}$
$2dw$	$0.25+0.1(\Delta C_L)^2$	$0.25+0.1(\Delta C_L)^2$
$w^2(1+d^2)$	$[0.2+0.1(\Delta C_L)^2]^2$	$[0.2+0.1(\Delta C_L)^2]^2$
e	$-0.6(\Delta C_L)^2$	$-0.6(\Delta C_L)^2$
$\Delta C_z(\alpha)$	$a_{0z}\alpha - C_{zs}(\alpha)$	

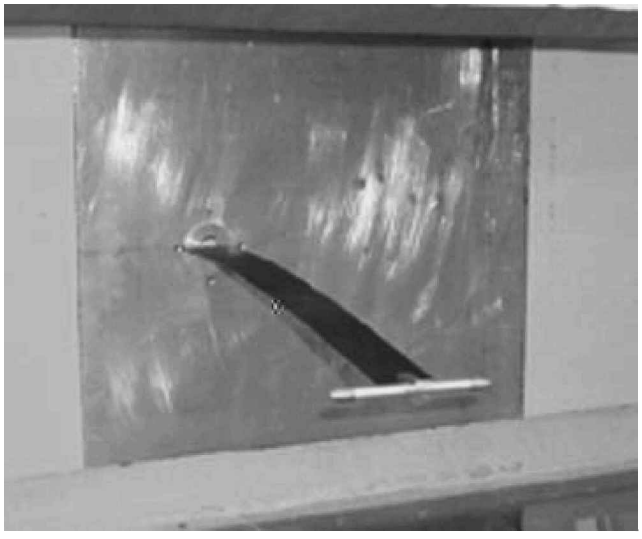

Fig. 1 Experimental model in the wind tunnel.

For the ONERA aerodynamic model, the lift, drag, and moment coefficients of each wing section in the differential equations are described in terms of a reduced time ($\mathrm{d}/\mathrm{d}\tau$, where $\tau = Ut/b$). However, this timescale is not convenient for the structural dynamic analysis of the wing. A more conventional differential operator relative to the real time, $\mathrm{d}/\mathrm{d}t$, is used in this paper for comparison with the experimental data. This is given by

$$\frac{\mathrm{d}(\,)}{\mathrm{d}\tau} = \frac{b}{U}\frac{\mathrm{d}(\,)}{\mathrm{d}t} = t_\tau(\cdot), \qquad t_\tau = \frac{b}{U}$$

The ONERA airfoil equations are given by

$$C_z = C_{z1} + C_{z2} \tag{3}$$

$$C_{z1} = t_\tau s_z \dot{\alpha} + t_\tau^2 k_{vz}\ddot{\phi} + C_{z\gamma} \tag{4}$$

$$t_\tau \dot{C}_{z\gamma} + \lambda_z C_{z\gamma} = \lambda_z(a_{0z}\alpha + t_\tau\sigma_z\dot{\phi}) + \alpha_z\left(t_\tau a_{0z}\dot{\alpha} + t_\tau^2\sigma_z\ddot{\phi}\right) \tag{5}$$

$$t_\tau^2\ddot{C}_{z2} + 2t_\tau dw\dot{C}_{z2} + w^2(1+d^2)C_{z2} = -w^2(1+d^2)\left(\Delta C_z + t_\tau e\frac{\partial \Delta C_z}{\partial\alpha}\dot{\alpha}\right) \tag{6}$$

C_z is either the relevant nondimensional lift force coefficient C_l and/or the pitch moment coefficient C_m. For the coefficients associated with Eqs. (3–6), see Table 1 (also Ref. 8). The moment is taken about the wing quarter-chord. The nondimensional drag force coefficient C_d is represented as $C_d = 0.008 + 0.003\alpha\dot{\alpha}$.

The aerodynamic coefficients C_l, C_d, and C_m are dependent on the angle of attack and the structural generalized coordinates in the ONERA aerodynamic model. The angle of attack α is expressed in a first harmonic form

$$\alpha = \alpha_0 + \alpha_s\sin\omega t + \alpha_c\cos\omega t \tag{7}$$

where α_0, α_s, and α_c depend on the structural motion and the steady-state angle θ_0.

The circulatory ($C_{z\gamma}$) and noncirculatory terms of the airfoil aerodynamics give the linear contribution C_{z1}, and the first harmonic form is given by

$$C_{z1} = C_{z10} + C_{z1s}\sin\omega t + C_{z1c}\cos\omega t \tag{8}$$

where C_{z10}, C_{z1s}, and C_{z1c} are linear functions of the structural motions.

The stalled (nonlinear) aerodynamic term C_{z2} is given by

$$C_{z2} = C_{z20} + C_{z2s}\sin\omega t + C_{z2c}\cos\omega t \tag{9}$$

where C_{z20}, C_{z2s}, and C_{z2c} are nonlinear functions of the structural motions due to the nonlinear deviation term ΔC_z in Eqs. (4–6).

For simplicity, following Dunn and Dugundji[8] and Kim and Dugundji,[9] ΔC_z is described by a single-breakpoint model based on low Reynolds number static experimental data for a NACA 0012 airfoil. Thus, a Fourier analysis of ΔC_z is used, and the first harmonic components of ΔC_z are obtained. The results are shown in Appendix A of Ref. 9. It is rewritten here.

For a single-breakpoint model,

$$\Delta C_z = \begin{cases} a_{11z}(\alpha - \alpha_\Delta) & \alpha \geq \alpha_\Delta \\ 0 & \alpha \leq \alpha_\Delta \end{cases} \tag{10}$$

$$\Delta C_{z0} = (a_{11z}/\pi)\Big[(\alpha_0 - \alpha_\Delta)\big\{\pi/2 - \tfrac{1}{2}(\varphi_\Delta + \varphi_{\Delta1})\big\} + (\alpha_v/2)(\cos\varphi_\Delta + \cos\varphi_{\Delta1})\Big] \tag{11}$$

$$\Delta C_{zs} = -(a_{11z}\alpha_v/\pi)\Big[\tfrac{1}{2}\sin\varphi_\Delta\cos\varphi_\Delta + \cos\varphi_{\Delta1}(\sin\varphi_\Delta - \sin\varphi_{\Delta1}) - \pi/2 - \tfrac{1}{2}(\varphi_{\Delta1} + \varphi_\Delta)\Big] \tag{12}$$

$$\Delta C_{zc} = (a_{11z}\alpha_v/\pi)\Big[\sin\varphi_\Delta\sin\varphi_{\Delta1} - \sin^2\varphi_\Delta + \tfrac{1}{4}(\cos 2\varphi_{\Delta1} - \cos 2\varphi_\Delta)\Big] \tag{13}$$

where

$$\varphi_\Delta = \begin{cases} \pi/2 & \text{if} \quad (\alpha_\Delta - \alpha_0)/\alpha_v > 1 \\ -(\pi/2) & \text{if} \quad (\alpha_\Delta - \alpha_0)/\alpha_v < -1 \\ \sin^{-1}[(\alpha_\Delta - \alpha_0)/\alpha_v] & \text{otherwise} \end{cases}$$

for no stall, full stall, and partial stall, respectively, and

$$\varphi_{\Delta1} = \begin{cases} \varphi_\Delta & \text{if} \quad (\alpha_\Delta - \alpha_0)/\alpha_v > 1 \\ \varphi_\Delta & \text{if} \quad (\alpha_\Delta - \alpha_0)/\alpha_v < -1 \\ \varphi_\Delta + 10\omega b/U & \text{otherwise} \end{cases}$$

for no stall, full stall, and partial stall, respectively, where $\alpha_v = \sqrt{(\alpha_s^2 + \alpha_c^2)}$ and α_Δ is the static stall angle of attack.

The nonlinear effect comes from the stall phases, φ_Δ and $\varphi_{\Delta1}$. Note that aerodynamic drag is not considered in the present paper. C_z only includes the lift C_l and pitching moment C_m.

Substituting Eqs. (2–13) into Eq. (1), a set of static equilibrium equations and of dynamic equations corresponding to sine and cosine terms is obtained. They are

$$\begin{bmatrix} K_0(U,\theta_0) & & \\ & M_{11}(U,\omega,\theta_0) & M_{12}(U,\omega,\theta_0) \\ & M_{21}(U,\omega,\theta_0) & M_{22}(U,\omega,\theta_0) \end{bmatrix}\begin{Bmatrix} X_0 \\ X_s \\ X_c \end{Bmatrix} + \begin{Bmatrix} Q_{N0} \\ Q_{Ns} \\ Q_{Nc} \end{Bmatrix} = \{0\} \tag{14}$$

where Q_{N0}, Q_{Ns}, and Q_{Nc} are nonlinear because ΔC_z is a nonlinear function of the angle of attack α.

Matrix equation (14) is solved via a Newton–Raphson method. Without loss of generality, the cosine component of the first torsion mode is set to zero. The remaining Fourier modal amplitudes and the oscillation frequency ω are then determined from the numerical solution.

Correlation Between Theory and Experiment

The experimental model includes two parts: a high-aspect-ratio wing with a slender body at the tip and a root support mechanism. The wing model is described in Ref. 5. The root support mechanism is a socket that allows a change of the steady angle of attack at the root. The root socket is mounted to the midpoint of side wall of the wind tunnel, as shown in Fig. 1.

A Helium–Neon laser, with 0.8 mw (microwatt) randomly polarized and 633-nm wavelength, is mounted on the top of the tunnel. The top of the tunnel is made of a glass plate with a thickness of 1.27 cm A mirror, 1.27 cm in diameter, is fixed on the tip of the wing. We use a mirror deflection technique to measure the tip static aeroelastic deflections of the wing. A point determined by a reflected light source is marked on readout grid paper placed on the top of the wind tunnel when the wing is undeflected. The readout grid paper is calibrated in the tip flap and twist deflections before the test. The reflected light source point with wing deflection as marked on the readout paper is then observed as the flow velocity is varied.

A microaccelerometer is mounted at the midspan of the wing to measure the LCO response of the wing. The output signals from these transducers are directly recorded on a computer with data acquisition and analysis software, Lab-VIEW version 5.1.

Static Aeroelastic Deflections of the Wing

The theoretical results are obtained from Eq. (14) using the harmonic balance approach. The flow velocity is varied from 1 to 38 m/s for the calculations and 10 to 36 m/s for the measurements. The wing is divided into 10 spanwise aerodynamic sections, that is, $NN = 10$. The stall aerodynamic data for a NACA 0012 airfoil are used in this paper. The structural modes selected are the first chordwise mode, first four flapwise modes, and first torsional mode. A Newton–Raphson method is used to solve the nonlinear algebraic equation (14).

The theoretical and experimental results are shown in Figs. 2a and 2b for a steady angle of attack $\theta_0 = 1$ deg. Figure 2a is for the tip flapwise deflection and Fig. 2b for the tip twist. The experimental data have some scatter due to the turbulent wind-tunnel aerodynamic noise, although the noise is small. A very high measurement sensitivity is obtained from the mirror technique. We use a bar in Fig. 2 to indicate the magnitude of the response uncertainty. As shown Fig. 2, both the tip and twist deflection increase with increasing flow velocity, but the tip deflection is always negative until the flow velocity reaches 34.5 m/s. At that velocity, the aerodynamic forces provide sufficient lift to overcome the effect of gravity. At $U > 34.5$ m/s, the system enters into the flutter instability range. The consequent LCO has a certain nonzero mean or temporal average. Also with LCO, aerodynamic stall occurs and the lift coefficient C_l has a large change in consequence. The experimental data fall near the theoretical curves in Fig. 2. In general, the agreement between theory and experiment is good except for some points at $U = 10$ and 15 m/s and in the higher flow velocity range. The data fluctuation increases due to greater aerodynamic turbulence and large LCO responses as the flow velocity increases.

Dynamic Aeroelastic Deflections of the Wing

The theoretical results are obtained from Eq. (14) using the harmonic balance approach. The flow velocity was varied from 33 to 38 m/s for the calculations and 31.4 to 36.5 m/s for the measurements. The theoretical and experimental results are shown in Figs. 3a and 3b for a steady angle of attack, $\theta_0 = 1$ deg, and at midspan of the wing. Figure 3a is for LCO flapwise amplitude. (Here we use rms values for comparison with the experimental results.) Figure 3b is the LCO frequency. The theoretical LCO responses are indicated by a solid line for a stable LCO or a broken line for an unstable

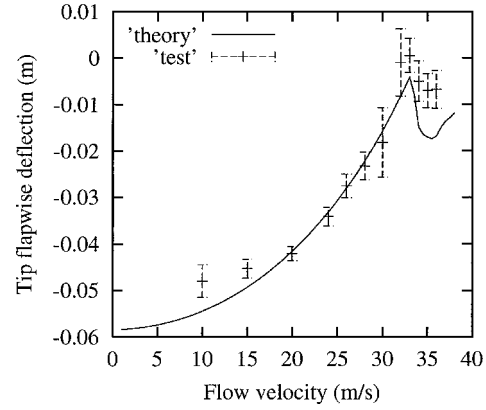

a) Flap deflection

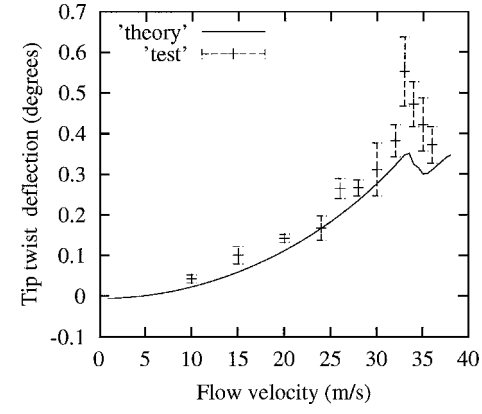

b) Twist deflection

Fig. 2 Static aeroelastic deflections of the wing vs flow velocity for pitch angle of attack $\theta_0 = 1$ deg.

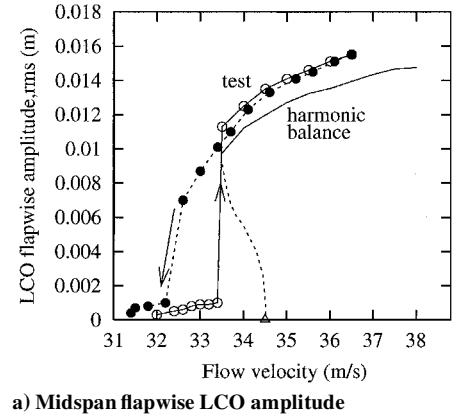

a) Midspan flapwise LCO amplitude

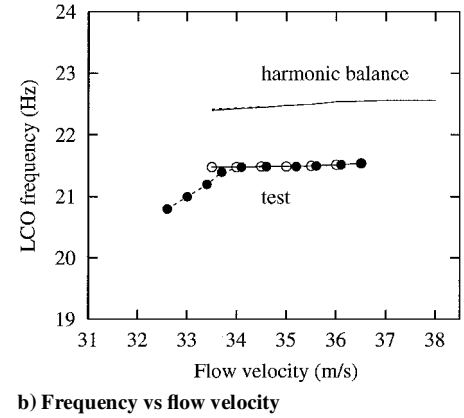

b) Frequency vs flow velocity

Fig. 3 Theoretical and experimental correlation for $\theta_0 = 1$ deg, ●, ○, test data; ——, - - - -, harmonic balance theoretical data; and △, linear flutter velocity.

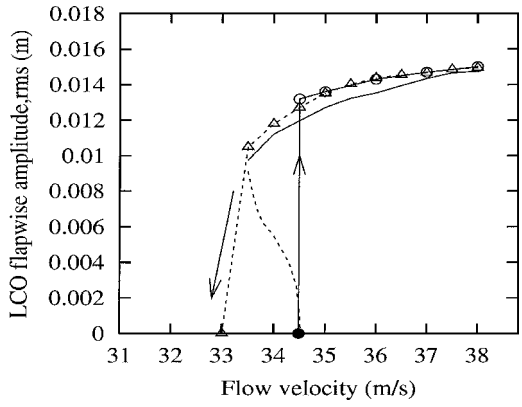

Fig. 4 Midspan flapwise LCO amplitude vs flow velocity for $\theta_0 = 1$ deg using harmonic balance method and time-marching approach: ○, △, time-marching results for increasing and decreasing flow velocity, respectively; ——, - - - -, harmonic balance results; and ●, linear flutter velocity.

LCO in Fig. 3a. There are two solutions that satisfy Eqs. (14) in the flow velocity range of $U = 33.5$–34.8 m/s. Thus, a hysteretic response is predicted by the harmonic balance solution. The linear flutter velocity that is calculated from the perturbation eigenvalue solution is also indicated in Fig. 3.

From the experimental measurement, we observed two different LCO responses for increasing and decreasing flow velocity. With increasing flow velocity, we find a jump at $U = 33.5$ m/s, which is similar to the theoretical results at $U = 34.5$ m/s as shown (Fig. 3). This velocity where the jump occurs is called the experimental flutter velocity. As the flow velocity increases further, the LCO amplitude as measured has a modestly larger increase than that found from theory. For model safety, the test was stopped at $U = 36.5$ m/s. When the flow velocity is decreased, we find another jump at $U = 32.4$ m/s as shown in Fig. 3a. The experimental LCO amplitudes for decreasing velocity are modestly smaller than those found for increasing velocity. The experimental amplitudes are taken as rms average values from a 50-s sampling interval. Very clear LCO hysteretic response is observed in the present wind-tunnel tests for the several different steady angles of attack.

The LCO frequency vs flow velocity is shown in Fig. 3b. The symbols used in Fig. 3b are the same as for Fig. 3a. As shown in Fig. 3b, the stable LCO frequency has a slight change as the flow velocity increases.

A hysteresis phenomenon was found from both the theoretical prediction and experimental observation. The theoretical/experimental agreement is reasonably good.

To further study the LCO hysteretic response, a time-marching approach was also used to solve Eq. (1). A typical LCO response (rms) vs flow velocity for $\theta_0 = 1$ deg and at the midspan position is shown in Fig. 4. The theoretical amplitudes are taken as rms average values from a 50-s sampling interval. For the increasing flow velocity case, the theoretical LCO occurs when the flow velocity is larger than the perturbation flutter velocity, and the amplitude has a jump from almost rest to a larger value. Once the onset of LCO occurs, the amplitude increases smoothly with increasing flow velocity. When $U > 38.6$ m/s, a numerical or possibly a physical divergence is found in the theoretical model. For the case of decreasing flow velocity, as shown by the broken line, the LCO amplitude decreases but does not exactly coincide with that for the increasing velocity case. Also, there is a jump in the LCO response at $U = 33.5$ m/s, which is a distinctly lower velocity than that found for the increasing velocity case, that is, $U = 34.5$ m/s.

To determine the source of the hysteresis, the theoretical calculation (time-marching approach) was repeated with the structural nonlinearity or the stall aerodynamic nonlinearity removed, alternatively. It is found the structural nonlinearity alone does not lead to hysteresis and LCO. However, the stall aerodynamic nonlinearity alone does give rise to hysteresis and LCO.

The two theoretical results (from the harmonic balance method and time-marching approach) as shown in Fig. 4 are very close. Thus, we conclude that the classical harmonic balance theory can be used to explain the LCO hysteresis phenomenon observed in the present nonlinear aeroelastic system.

Conclusions

The present experimental and theoretical results provide new insights into nonlinear aeroelastic phenomena for high-aspect-ratio wings (with a tip slender body) that have a beamlike structural behavior. An LCO hysteretic response is observed in the theoretical analysis as well as the experimental measurement. Both a time-marching approach (time domain) and a harmonic balance method (frequency domain) show this hysteresis phenomenon. The onset of the LCO hysteretic response is generally dependent on a delicate balance between stall aerodynamics and the structural nonlinear forces. However, the stall aerodynamics are dominant for the present experimental wing model.

Acknowledgments

This work was supported by the Defense Advanced Research Projects Agency through Air Force Office of Scientific Research Grant F49620-99-1-00253, "Aeroelastic Leveraging and Control Through Adaptive Structures" under the direction of Ephrahim Garcia and Dan Segalman. All numerical calculations were done on a supercomputer, T916, in the North Carolina Supercomputing Center.

References

[1]Hodges, D. H., and Dowell, E. H., "Nonlinear Equations of Motion for the Elastic Bending and Torsion of Twisted Nonuniform Rotor Blades," NASA TN D-7818, 1974.

[2]Patil, M. J., Hodges, D. H., and Cesnik, C. E. S., "Nonlinear Aeroelastic Analysis of Complete Aircraft in Subsonic Flow," *Journal of Aircraft*, Vol. 37, No. 5, 2000, pp. 753–760.

[3]Tang, D. M., and Dowell, E. H., "Effects of Geometric Structural Nonlinearity on Flutter and Limit Cycle Oscillations of High-Aspect Ratio Wings," *Journal of Fluids and Structures* (to be published).

[4]Patil, M. J., and Hodges, D. H., "On the Importance of Aerodynamic and Structural Geometrical Nonlinearities on Aeroelastic Behavior of High-Aspect-Ratio Wings," AIAA Paper 2000-1448, April 2000.

[5]Tang, D. M., and Dowell, E. H., "Experimental and Theoretical Study on Flutter and Limit Cycle Oscillations of High-Aspect-Ratio Wings," *AIAA Journal*, Vol. 39, No. 8, 2001, pp. 1430–1441.

[6]Tang, D. M., and Dowell, E. H., "Experimental and Theoretical Study of Gust Response for a High-Aspect-Ratio Wing," *AIAA Journal*, Vol. 40, No. 3, 2002, pp. 419–429.

[7]Tran, C. T., and Petot, D., "Semi-Empirical Model for the Dynamic Stall of Airfoils in View to the Application to the Calculation of Responses of a Helicopter Blade in Forward Flight," *Vertica*, Vol. 5, No. 1, 1981, pp. 35–53.

[8]Dunn, P., and Dugundji, J., "Nonlinear Stall Flutter and Divergence Analysis of Cantilevered Graphite/Epoxy Wings," *AIAA Journal*, Vol. 30, No. 1, 1992, pp. 153–162.

[9]Kim, T., and Dugundji, J., "Nonlinear Large Amplitude Aeroelastic Behavior of Composite Rotor Blades," *AIAA Journal* , Vol. 31, No. 8, 1993, pp. 1489–1497.